The Hidden Diversity of Vascular Patterns in Flower Heads

Andrew Owens, Teng Zhang, Philmo Gu, Jeremy Hart, Jarvis Stobbs,
Mikolaj Cieslak, Paula Elomaa, Przemyslaw Prusinkiewicz

Supplemental Model Description

1 Overview

To propose a plausible mechanism of vascular patterning in flower heads and obtain insights regarding possible sources of pattern diversity, we reproduced key features of the vascular patterns in Bellis, sunflower, and gerbera heads using a parametrized dynamic computational model (Fig. SMD1). Inputs to the final stage of this model, which outputs the vascular pattern (V-Model), are a model of phyllotaxis (P-model) and a volumetric model of receptacle growth that includes the receptacle interior (G-model). The P-model simulates the dynamic patterning of bract and floret primordia, which the vascular strands will reach. The G-model simulates the expansion of space within which the vascular pattern emerges and deforms as the receptacle grows, using a sequence of shape-dependent coordinate systems calculated by the H-model. Both the P-model and the H-model rely on a data-driven model of receptacle contour expansion (C-model).
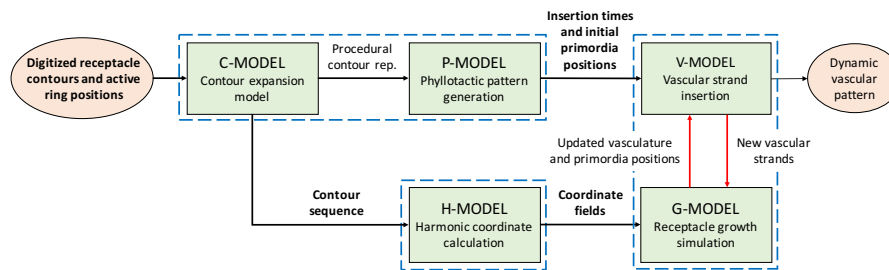
Figure SMD1: Data flow in the dynamic model of vascular patterning in heads. Dashed lines indicate model components implemented as separate programs. Bold font indicates data exchanged as files. Red arrows highlight the main iteration loop.

The simulation of vascular system development is preceded by preprocessing steps. First, receptacle contours and active ring positions measured at discrete time points during head development are interpolated by the C-model to describe the receptacle contour and the position of the active ring as continuous functions of time (Sec. 2). Both of these functions are employed by the model of phyllotaxis (P-model) to generate time-stamped initial primordia positions on the growing receptacle (Sec. 3). In addition, the H-model uses a sequence of receptacle contours output by the C-model to create a corresponding sequence of the entire receptacle sections, including their interior (Sec. 4.2). The development of the vascular system is then simulated iteratively, in a loop consisting of two operations taking place over incrementally advancing time:

- Insertion of new vascular strands (V-model) (Sec. 5). Typically, these strands are induced by the addition of new primordia and connect them to the existing vasculature (initially, the procambial ring at the base of the receptacle). Consistent with our observations, the gerbera model also incorporates centripetally extending adaxial strands, which support floret veins formed later.

- Receptacle growth (G-model) (Sec. 4.3). This operation entails incremental deformation of all strands embedded in the growing receptacle, as well as the repositioning of primordia on the receptacle surface due to the growth of the receptacle over a simulation step.

The simulation process is illustrated in Fig. SMD2.
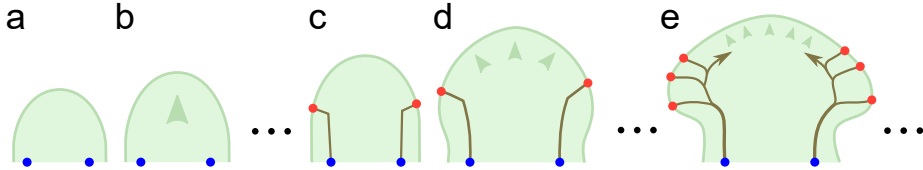
Figure SMD2: Simulation process in a section of a head. (**a**) Initialization. A receptacle (green) and procambial ring (blue dots) are established. (**b**) Receptacle growth. Initially no primordia or vascular strands are present. (**c**) Patterning. New primordia (red) are positioned on the receptacle surface according to the P-model, and strands (brown) connecting these primordia to the procambial ring are established by the V-model. (**d**) Next growth step. Vascular strands embedded in the receptacle are deformed, and primordium positions on the receptacle surface are adjusted by the G-model as the receptacle grows. (**e**) Result of iterating steps (c) and (d) several times. As the simulation progresses, new primordia emerge, giving rise to strands that connect these primordia to the procambial ring or to the strands formed previously. Arrows indicate additional adaxial strands specific to gerbera.

2 The contour expansion model (C-model)

The C-model produces a continuous-time description of the expanding receptacle contour by interpolating digitized profiles of receptacles scanned at different stages of development (Fig. S9a,d,g). For each plant species, it is constructed by following the steps described by Zhang et al. (2021):

1. Volumetric scanning of several (7–10) heads capturing head development from an early stage to the stage at which all primordia and vascular strands have been patterned;

2. Extraction of a virtual longitudinal section of each scan;

3. Manual tracing of the contour of each section, including positions of selected primordia serving as landmarks, and the boundary of the phyllotactic pattern defining the morphogenetically active zone;

4. Interpolation of these data.

3 The phyllotactic patterning model (P-model)

The P-model operates on the receptacle surface obtained by revolving the receptacle contour around the head axis (Fig. S9b,e,h). To generate the phyllotactic pattern in a gerbera head, we used the model described by Zhang et al. (2021), augmented with the information on the fate of floret primordia (trans vs. disc) (Fig. S19c). To generate the phyllotactic patterns in sunflower and Bellis heads (Fig. S9f,i) we modified the gerbera model by using C-models of receptacle contour expansion based on the sunflower and Bellis data, and sizes of primordia estimated from measurements of sunflower and Bellis heads.

4 The receptacle model (H and G-models)

4.1 Overview

Our data consist of 3D scans of heads at different developmental stages, as opposed to time-lapse images of the same developing head. With these data we were able to identify primordia that served as landmarks for determining local growth rates of the receptacle surface, but we were unable to identify internal landmarks that would provide information on the local growth within the head. Consequently, we approximated the growth of the receptacle interior on the basis of the expansion of its surface.

We assume that the receptacle grows in a radially symmetric manner. It is thus sufficient to simulate the growth of one half of a single longitudinal cross-section only, since all sections grow the same way and can be obtained by rotating a single (half-)cross-section around the head axis (Fig. S9a,b,d,e,g,h). We conceptualize this cross-section as a (visco)elastic membrane attached to the

section contour, although in our model it is defined in geometric rather than physical terms. In each simulation step the contour expands as described by the C-model, slightly deforming the membrane attached to it. This deformation changes the positions of points embedded in the membrane — and thus in the interior of the receptacle — including those representing the developing vascular system.

Mathematically, our model of the receptacle interior growth (G-model) is based on caging: the idea of smoothly deforming complex objects by embedding them into a geometric structure — the cage — manipulated with a small number of control points (Joshi et al., 2007). A historical predecessor to caging is the transformation method proposed by Thompson (1942) to describe how organisms change their shape during evolution or development. With that method, the shape of interest was positioned in a Cartesian coordinate system and deformed through linear or non-linear transformations of this system. Instead, to model the growth of the receptacle interior we employ harmonic coordinates: a flexible generalization of barycentric coordinates allowing for an arbitrary number of control points to be placed on the receptacle contour (Joshi et al., 2007). As the control points move due to contour expansion, points with given coordinates follow along, simulating the growth of the receptacle interior.

4.2 Calculation of harmonic coordinates (H-model)

Let Ω denote one half of the receptacle cross-section, and $\partial\Omega$ be the boundary of Ω. We partition this boundary into segment Γ representing the contour, and segment Γ_m that closes $\partial\Omega$ along the head axis (Fig. SMD3):
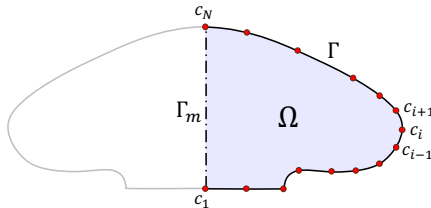
Figure SMD3: Elements of a receptacle cross-section representation.

Assume that Γ is defined by a set of control points $\mathbf{c}_i \in \Gamma$, $i = 1, ..., N$. Some of these points match landmarks such as bracts, and others may be inserted in-between to ensure sufficiently precise contour representation. Following Joshi et al. (2007), the position of an arbitrary point $\mathbf{p} \in \Omega$ can be defined as the affine combination (Goldman, 2002) of the control point positions,

$$\mathbf{p} = \sum_{i=1,...,N} w_i(\mathbf{p})\mathbf{c}_i, \tag{1}$$

in which weight fields (functions $w_i : \Omega \to [0,1]$) are solutions to Laplace's equation,

$$\nabla^2 w_i = 0. \tag{2}$$

Each field w_i, $i = 1, \ldots, N$, is calculated assuming boundary conditions (BC):

(Dirichlet BC) $$w_i(\mathbf{c}_j) = \delta_{i,j}, \qquad\qquad j = 1, \ldots, N, \quad (3)$$

(Neumann BC) $$\nabla w_i(\mathbf{p}) \cdot \hat{\mathbf{n}} = 0, \qquad\qquad \mathbf{p} \in \Gamma_m, \quad (4)$$

where $\delta_{i,j}$ is the Kronecker delta function:

$$\delta_{i,j} = \left\{ \begin{array}{ll} 1 & \text{if } i = j, \\ 0 & \text{if } i \neq j. \end{array} \right. \qquad (5)$$

Taking Equation 5 into account, boundary condition (3) specifies that weight field w_i evaluates to 1 at control point $\mathbf{c}_i$ and to 0 at all remaining control points. It also implies that weights $w_1(\mathbf{p}), \ldots, w_N(\mathbf{p})$ of any point $\mathbf{p} \in \Omega$ sum to 1, as required by the definition of the affine combination of points. Boundary condition (4) ensures that all points on the head axis Γ_m remain on the axis, as a move across or away from the axis would violate the assumption of head symmetry. The N-tuple of weights $w_1(\mathbf{p}), \ldots, w_N(\mathbf{p})$ constitutes harmonic coordinates of point $\mathbf{p}$. They are sample values of the harmonic coordinate fields $w_1, \ldots, w_N$ at point $\mathbf{p}$.

We solve Laplace's equation numerically for each contour in the developmental sequence produced by the C-model. To this end, we first (Delaunay) triangulate the Ω domain using the `Triangle` library (Shewchuk, 1996). Laplace's equation is then discretized for this triangulation using the cotangent formula (Crane et al. 2013, see also Ringham et al. 2021) implemented in the `libigl` library (Jacobson et al., 2018). This discretization yields a system of linear equations associated with the triangle vertices (Jacobson, 2013), which we solve using the simplicial Cholesky factorization algorithm in the `eigen` library (Guennebaud et al., 2010). This computation is repeated for all N different boundary conditions (choices of control point $\mathbf{c}_i$ at which the weight field is equal to 1), yielding N weight fields $w_1, \ldots, w_N$. The results are stored in the coordinate fields file, on which the receptacle growth model (G-model) subsequently relies (Fig. SMD1).

Three examples of weight fields w_i are shown in Fig. SMD4. Weight values for points $\mathbf{p}$ inside the triangles were calculated by linearly interpolating the weights at the triangle vertices using barycentric coordinates (Anisimov et al., 2016). Consistent with the membrane analogy, each control point $\mathbf{c}_i$ affects weights $w_i(\mathbf{p})$ of points $\mathbf{p}$ positioned close to it more strongly than weights of points $\mathbf{p}$ positioned further away.

4.3 The receptacle growth model (G-model)

The input to the receptacle growth model is a sequence of $M + 1$ harmonic coordinate fields $w_1^t, \ldots, w_N^t$ representing snapshots of the receptacle development at time steps $t = 0, \ldots, M$, where M is the number of simulation steps. We decrease the simulated time interval between consecutive steps t as the receptacle grows, because the geometry of larger receptacles changes faster than the geometry of receptacles at the onset of their development.

5
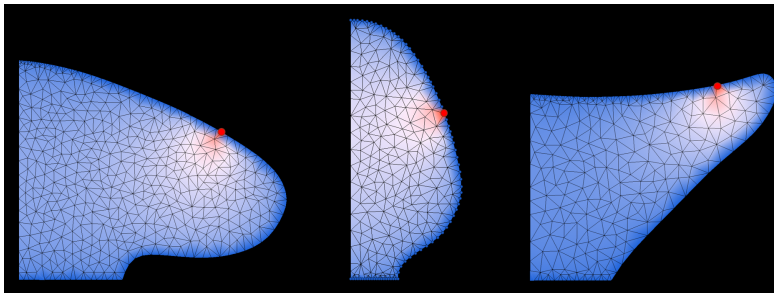
Figure SMD4: Three examples of harmonic weight fields associated with receptacle sections. The influence of the selected point c_i (red) on field w_i is the highest (red) close to c_i and decreases (white to blue) further away.

With these harmonic coordinate fields in place, the propagation (change of position) of a point $\mathbf{p} \in \Omega^t$ resulting from the receptacle growth from stage t to stage $t+1$ is modelled by expressing its position at time t, $\mathbf{p}^t$, using harmonic coordinate values (weights) $w_i^t(\mathbf{p}^t)$ associated with section Ω^t, and using the same values for the subsequent section Ω^{t+1} (Joshi et al., 2007):

$$\mathbf{p}^{t+1} = \sum_{\mathbf{c}_i^{t+1} \in \Omega^{t+1}} w_i^t(\mathbf{p}^t)\mathbf{c}_i^{t+1}. \tag{6}$$

As the control points move, point $\mathbf{p}$ will move in a "shape-aware" manner, i.e., its position will be most strongly affected by the contour points nearby.

Harmonic coordinates are well suited for both convex and concave control cages, but large deformations from convex to concave configurations may reposition some interior points $\mathbf{p} \in \Omega^t$ outside receptacle domain Ω^{t+1}. With small time steps, the changes in the receptacle shape between stages t and $t+1$ are also small, and we have rarely encountered this problem in practice. Nevertheless, we test for its occurrence, and if it happens, we project the misplaced point to its nearest location in contour $\partial\Omega^{t+1}$.

5 The vascular patterning model (V-model)

5.1 Background

In constructing the vascular model we assumed that the basic processes of vascular patterning in heads are similar to those analyzed in inflorescences of plants not forming heads, such as Arabidopsis, tomato and Brachypodium (Reinhardt et al., 2003; Bayer et al., 2009; O'Connor et al., 2014). In brief, as the meristem grows, maxima of auxin concentration emerge in the active (peripheral) zone of the epidermis through feedback between auxin transport and the positions of PIN1 auxin efflux carriers. These maxima are sources of auxin flowing towards previously formed vascular strands, acting as sinks. Following the canalization

hypothesis (Sachs 1969, 1991), the flow of auxin is patterned into narrow streams or canals, along which the vascular tissues differentiate. Experimental evidence for the above processes has been supported by cell-level computational models, which simulate the formation of auxin maxima in the epidermis (Smith et al., 2006; Jönsson et al., 2006) and the formation of canals of auxin flow between sources and sinks (Mitchison, 1980; Rolland-Lagan and Prusinkiewicz, 2005), and integrate both processes (Bayer et al., 2009; O'Connor et al., 2014); see (Cieslak et al., 2022) for a recent review).

Modeling large multicellular structures at the cellular level is a computationally daunting task. Consequently, models abstracting cell-level processes into higher-level geometric constructs have been proposed to simulate vascular patterning of entire plant organs (Cieslak et al., 2022). In the particle-based model introduced for leaves by Rodkaew et al. (2002, 2003) and extended to developing inflorescences by Owens et al. (2016), vascular strands originate at the organ periphery, then extend towards the organ base by the addition of short segments ("particles") at the vein tips. With the space colonization algorithm proposed by Runions et al. (2005), leaf veins also extend by the addition of short segments, but patterning proceeds in the opposite direction: from the leaf base towards its margin. These dynamics are simplified further in the resistance minimization model proposed by Runions et al. (2017), in which entire vein segments connecting auxin sources to the previously formed vasculature are inserted in single simulation steps. Our model of vascular patterning in flower heads is based primarily on the resistance minimization algorithm, which is well suited to simulated experiments and refinements (Runions et al., 2017).

5.2   Vascular strand representation

We model vasculature as a directed graph $\langle \mathcal{V}, \mathcal{E} \rangle$ with vertices $\mathbf{v} \in \mathcal{V}$ connected by edges $\mathbf{e} \in \mathcal{E}$. The edges represent segments of vascular strands, and the vertices represent points at which these segments meet. Some vertices may represent branching or joint points of several strands, while others may represent connecting points between short segments of a longer strand. The ground tissue is not represented explicitly and is defined by the absence of vasculature. The impact of receptacle growth on the shape of vascular strands is approximated by expressing positions of all vertices $\mathbf{v}$ using harmonic coordinates, which deform as the receptacle expands. Intuitively, we may thus think of the harmonic coordinate fields as playing the role of the ground tissue, in which the vasculature is embedded. Note, however, that the harmonic coordinates of all vertices are recomputed after each growth step, and thus the mathematical description of this embedding changes from one step to the next.

5.3   Vein initials

The patterning of each vascular strand begins with the placement of a primordium on the receptacle surface by the phyllotaxis model (P-model). This placement is followed by the formation of a short vein initial that penetrates the

7

receptacle interior in a direction approximately normal to the receptacle surface. Biologically, it may originate in the supported bract or flower, and extend into the subepidermal tissue, where it connects to other strands of the emerging vascular network. In the following description we refer to this connecting point as the primordium, even though it is at some distance from the actual primordium returned by the P-model.

5.4   Minimum resistance path

Once a primorium $\mathbf{p}$ has been established, a strand segment that connects it to the already existing vasculature is formed. The connecting vertex $\mathbf{v}$ is chosen such that the resistance between the primordium and the procambial **ring** located at the receptacle base is minimized:

$$\mathbf{v} = \operatorname*{argmin}_{\mathbf{v}' \in \mathcal{V}} \left[R_{\mathcal{G}}(\mathbf{p}, \mathbf{v}') + R_{\mathcal{V}}(\mathbf{v}', \mathbf{ring}) \right]. \tag{7}$$

Here $R_{\mathcal{G}}(\mathbf{p}, \mathbf{v}')$ is the resistance of the path from primordium $\mathbf{p}$ to a "candidate" vertex $\mathbf{v}'$ passing through the ground tissue, and $R_{\mathcal{V}}(\mathbf{v}', \mathbf{ring})$ is the resistance of the path from $\mathbf{v}'$ to the procambial **ring** passing through the already differentiated vascular strands. While modeling leaf vasculature, Runions et al. (2017) assumed that resistance $R_{\mathcal{G}}(\mathbf{p}, \mathbf{v}')$ was proportional to the (Euclidean) distance $\mathrm{d}(\mathbf{p}, \mathbf{v}')$ between points $\mathbf{p}$ and $\mathbf{v}'$:

$$R_{\mathcal{G}}(\mathbf{p}, \mathbf{v}') = r_{\mathcal{G}} \, \mathrm{d}(\mathbf{p}, \mathbf{v}'), \tag{8}$$

where $r_{\mathcal{G}}$ is the resistivity (resistance per unit distance) of the ground tissue. Similarly, the resistance $R_{\mathcal{V}}(\mathbf{v}', \mathbf{ring})$ between point $\mathbf{v}'$ and the **ring** through the existing vasculature $\mathcal{V}$ was calculated as

$$R_{\mathcal{V}}(\mathbf{v}', \mathbf{ring}) = r_{\mathcal{V}} \sum_{\mathbf{e} \in \mathcal{E}_{\mathbf{v}'}} l_{\mathbf{e}}, \tag{9}$$

where $r_{\mathcal{V}}$ is the resistivity of vascular strands, and $l_{\mathbf{e}}$ denotes the length of the strand segment $\mathbf{e}$ in the path $\mathcal{E}_{\mathbf{v}'}$ connecting vertex $\mathbf{v}'$ to the procambial **ring**.

Equations 8 and 9 imply that resistivities of the ground tissue ($r_{\mathcal{G}}$) and vascular strands ($r_{\mathcal{V}}$) are constant scalar values. With this assumption it is possible to simulate vascular development in diverse leaves (Runions et al., 2017), but to reproduce vascular patterns in heads we needed to vary resistivities according to time and direction.

5.5   Time dependence

Vascular strands supporting the first few bracts in all three modeled species run approximately parallel to each other (Figs. 5 and S6b). To promote direct connections of these bracts to the procambial ring without forming a branching structure, we assumed that the ground tissue resistivity $r_{\mathcal{G}}$ is low in very young

heads. It increases to its target value used in the remainder of the simulation after the first few strands have been patterned.

An inherent feature of spiral phyllotaxis is that primordia are arranged into parastichies: conspicuous spirals running in opposite directions. In some flower heads, such as Bellis, developing vascular strands consistently follow a specific parastichy family (Fig. 5i). In contrast, strands simulated using the minimum resistance algorithm with constant resistivities switch their course between different parastichies in an irregular manner (Fig. S10a). To simulate the development of vascular strands that follow a specific family of parastichies, we extend the minimum resistance model by assuming that ground tissue resistivity $r_{\mathcal{G}}$ and vascular strand resistivity $r_{\mathcal{V}}$ depend locally on time in a manner promoting connections to older strands. Specifically, ground tissue resistivity $r_{\mathcal{G}}(\mathbf{p}, \mathbf{v}')$ adjusted for the age of nearby veins is calculated using the formula

$$r_{\mathcal{G}}^{age}(\mathbf{p}, \mathbf{v}') = r_{\mathcal{G}} + \mu_{age} \left[\frac{\max_{\mathbf{u} \in S_{\mathbf{p}}}\{age(\mathbf{u})\}}{age(\mathbf{v}')} - 1 \right], \tag{10}$$

where $S_{\mathbf{p}}$ is a set of vertices $\mathbf{u}$ close to vertex $\mathbf{p}$. Resistivity $r_{\mathcal{G}}^{age}(\mathbf{p}, \mathbf{v}')$ is thus increased with respect to the reference value $r_{\mathcal{G}}$ for vertices $\mathbf{v}'$ younger than the oldest vertex $\mathbf{u}$ in proximity of $\mathbf{p}$. Correspondingly, Equation 8 is modified to

$$R_{\mathcal{G}}(\mathbf{p}, \mathbf{v}') = r_{\mathcal{G}}^{age}(\mathbf{p}, \mathbf{v}') \, \mathrm{d}(\mathbf{p}, \mathbf{v}'). \tag{11}$$

Resistivity of an existing strand $\mathbf{e}$ is assumed to change from the ground tissue resistivity $r_{\mathcal{G}}$ to its final value $r_{\mathcal{V}}$ over maturation time τ_m. This change is effected using a sigmoidal function $r_{\mathcal{V}}^{age}(\mathbf{e})$ of the segment age measured from the time of the segment creation. Equation 9 is thus modified to:

$$R_{\mathcal{V}}(\mathbf{v}', \mathbf{ring}) = \sum_{\mathbf{e} \in \mathcal{E}_{\mathbf{v}'}} r_{\mathcal{V}}^{age}(\mathbf{e}) \, l_{\mathbf{e}}. \tag{12}$$

Taking the time-dependent resistivities into account, the path of least resistance is found by substituting Equations 11 and 12 into Equation 7. An example of a vascular system following a single family of parastichies obtained in this manner is shown in Fig S10b.

5.6   Reticulation

To complete the reticulate vasculature exemplified by Bellis, the vascular connections that correspond to the opposite family of parastichies must also be produced. Data (Fig. 5c) indicate that these connections are formed after strands from the first family of parastichies, as opposed to appearing concurrently. We find them by searching for the minimum-resistance connection using Equation 7 again, after a delay τ_d, while excluding vertices $\mathbf{v}'$ that already belong to the previously formed vascular strand originating at $\mathbf{p}$. Once a candidate vertex $\mathbf{v}$ has been found, the total resistance $R(\mathbf{p}, \mathbf{ring})$ of the path passing through $\mathbf{v}$ is compared to the resistance of the original path. Unless the resistance of the

new path is disproportionally high (the ratio of the resistances of the new and old paths is above a predefined threshold κ), the connection is made. The effect of this process is illustrated in Fig. S10c.

5.7 Sectoriality

In sunflower heads, vascular strands supporting floret primordia penetrate the receptacle deeply, forming highly branching tree-like structures attached to the radially spreading abaxial strands. These tree structures extend sectorially, which gives them an almost two-dimensional character. We account for this sectoriality by assuming the presence of a mechanism that polarizes the ground tissue radially, producing an anisotropic resistivity field. To model it, we extend the minimum resistance framework by introducing a non-linear function that increases ground tissue resistivity $r_\mathcal{G}(\mathbf{p}, \mathbf{v}')$ as point $\mathbf{v}'$ deviates from the longitudinal section $\mathbf{p}$ occupies. Some degree of sectoriality is also observed in other heads; the impact of its magnitude is illustrated in Fig. S11.

We use the perpendicular distance between $\mathbf{v}'$ and the radial longitudinal sector including $\mathbf{p}$ to modulate ground tissue resistivity $r_\mathcal{G}(\mathbf{p}, \mathbf{v}')$

$$r_\mathcal{G}^{sec}(\mathbf{p}, \mathbf{v}') = r_\mathcal{G}\left(1 + \mu_{sec}\left[\hat{\mathbf{n}} \cdot (\mathbf{v}' - \mathbf{p})\right]^2\right),\tag{13}$$

where $\hat{\mathbf{n}}$ is the normal of the sector including $\mathbf{p}$. Parameter μ_{sec} thus controls the increase of ground tissue resistivity in directions not aligned with the longitudinal sector; $\mu_{sec} = 0$ disables this feature. Sectoriality can be combined with time dependence by replacing $r_\mathcal{G}$ in Eq. 10 with the function $r_\mathcal{G}^{sec}(\mathbf{p}, \mathbf{v}')$ (Eq. 13).

5.8 Adaxial vascular strands of gerbera

A distinctive feature of gerbera heads is the presence of adaxial strands that originate near the head rim and extend radially towards the head center (Figs. 2b,c and S1b,c). These strands have a different character from both the Bellis strands, which follow parastichies, and the sunflower strands, which form branching structures deeply penetrating the receptacle. Remarkably, the adaxial strands of gerbera develop ahead of the florets they support, which indicates that their development is not guided by the floret primordia (Figs. 5b,c and S5d). To model these strands, we assume the presence of a diffuse auxin source, represented geometrically as a set of "attraction points", towards which the adaxial strands gradually extend. The attraction points are distributed subepidermally ahead of the active ring, such that they maintain constant density. The strand extension process is simulated using the space colonization algorithm (Runions et al., 2005, 2007). The veins connecting florets to the already formed vasculature are then patterned using the resistance minimization algorithm, taking the already formed adaxial strands into account.

10

5.9 Randomization

Single-shot vascular connections generated by the resistance minimization algorithm are straight lines connecting primordia (more precisely, the ends of vein initials originating at the primordia) to the existing vasculature. In contrast, the strands observed in heads meander, deviating from straight lines to various degrees. One source of these deviations is the irregular lattice of ground tissue cells within which the strand patterning and differentiation occur. As our geometric model is an abstraction that does not explicitly simulate ground tissue cells or other possible factors in path deviation (except for the random distribution of attraction points inherent in the space colonization algorithm), we introduce deviations by randomly perturbing the vascular paths. To this end, we build a strand from $\mathbf{p}$ to $\mathbf{v}$ as a polygonal line with segments of approximately equal length δ_{step} joined at vertices $\mathbf{p}_0 = \mathbf{p}, \mathbf{p}_1, \mathbf{p}_2, \ldots, \mathbf{p}_n = \tilde{\mathbf{v}}$. The endpoint $\tilde{\mathbf{v}}$ is an existing vascular vertex in the proximity of, but not necessarily coinciding with, $\mathbf{v}$. The process is controlled by two parameters: the probability η that a perturbation will take place, and the maximum magnitude of this perturbation, γ_{max}. The polygonal trajectory is constructed according to the formula:

$$\mathbf{p}_{t+1} = \begin{cases} \mathbf{p}_t + \delta_{step}\left(\hat{\mathbf{s}}_t + \gamma_t \hat{\mathbf{d}}_t\right) & \text{with probability } \eta, \\ \mathbf{p}_t + \delta_{step}\hat{\mathbf{s}}_t & \text{otherwise,} \end{cases} \tag{14}$$

where $\hat{\mathbf{s}}_t$ is the unit vector from vertex $\mathbf{p}_t$ towards the target vertex $\mathbf{v}$, $\hat{\mathbf{d}}_t$ is a randomly chosen direction of deviation perpendicular to $\hat{\mathbf{s}}_t$ (in 3D), and γ_t is the magnitude of this deviation, chosen randomly (with uniform distribution) from the interval $[0, \gamma_{max}]$. The strand construction ends when the most recently constructed vertex $\mathbf{p}_t$ is within a predefined threshold distance from a vertex $\tilde{\mathbf{v}}$ of the existing vasculature, at which time the connection is completed by adjusting position of $\mathbf{p}_t$ to coincide with $\tilde{\mathbf{v}}$.

5.10 Calculation of strand diameter

The model elements described so far are focused on generating the skeletons of vascular structures. To facilitate visual comparisons between scanned and simulated patterns, we also model the widths (diameters) of the vascular strands. We adapt for this purpose the method proposed for leaf venation by Runions et al. (2005). The computation proceeds basipetally, from the organ primordia to the receptacle base. Veins directly supporting organ primordia, as well as the tips of adaxial strands in gerbera, are assigned predefined widths ρ specified as model parameters. Vascular segments that extend a strand outside of branching points have the same diameter as the preceding strands. At the points where strands with diameters d_1 and d_2 meet in their course toward the receptacle base, diameter d_{12} of the resulting, more basal strand is calculated using Murray's (1927) law,

$$d_{12}^n = d_1^n + d_2^n, \tag{15}$$

where n is a model parameter (MacDonald, 1983). These rules suffice to determine strand widths in open vascular patterns (without loops).

In the reticulated vasculature of Bellis (Fig. 7) and its less regular variants (Fig. S11), we also consider configurations in which vascular strands split. While modeling leaf venation, Runions et al. (2005) assumed that veinlets reaching a reticulation point contribute evenly toward the width of the outgoing strands. In the model of Bellis, we modify this heuristic by assuming that the strand or strands reaching a reticulation point contribute to the width of outgoing strands unevenly, favoring the outgoing strand that was formed first. This asymmetry results in different diameters of the strands following opposite parastichies (Fig. 7), as observed in nature (Fig. 3g).

A   Appendix

Parameter	Bellis	Sunflower	Gerbera
C-Model: Contour expansion model (Sec. 2)			
Number of longitudinal sections	7	9	10
Number of landmarks	40	60	40
Final head height	8.37	5.35	7.65
Final head diameter	7.19	12.79	18.72
P-Model: Phyllotactic pattern generation (Sec. 3)			
Numbers of primordia	Bract 28 Floret 392	Bract 81 Floret 416	Bract 84 Trans 167 Disc 466
H-Model and **G-Model**: Receptacle model (Sec. 4)			
Number of control points N	71	99	110
Number of contours $M+1$	2,214	2,214	2,214
Number of simulation iterations	2,214	2,214	2,214
Total number of fields w_i^t	157,194	219,186	243,540
V-Model: Vasculature strand insertion (Sec. 5)			
Final number of vertices $|\mathcal{V}|$	14,172	38,598	47,497
Minimal resistance path (Sec. 5.4)			
Reference ground resistivity $r_{\mathcal{G}}$	$0.5 \to 6.5$	$0.6 \to 2.1$	$0.4 \to 7.0$
Final strand resistivity $r_{\mathcal{V}}$	1.0	1.0	1.0
Time dependence (Sec. 5.5)			
Ground resistivity control μ_{age}	1.0	0.0	0.0
Maturation time τ_m [iterations]	255	4	13
Reticulation (Sec. 5.6)			
Delay τ_d [iterations]	285	N/A	N/A
Threshold κ	1.3	N/A	N/A
Sectoriality (Sec. 5.7)			
Sectoriality control μ_{sec}	0	0.65	0.25
Adaxial vascular strands (Sec. 5.8)			
Attraction points (max.)	N/A	N/A	1065
Randomization (Sec. 5.9)			
Segment length δ_{step}	0.02	0.01	0.02
Deviation probability η	30%	49%	30%
Maximum deviation γ_{max}	0.3	0.8	0.27
Calculation of strand diameter (Sec. 5.10)			
Diameter ρ	Bract 0.08 Floret 0.04	Bract 0.14 Floret 0.1	Bract 0.14 Floret 0.09 Adaxial 0.11
Murray's law exponent n	5	5	5

Table SMD1: Numerical values of key model parameters used in the simulations of the Bellis, sunflower and gerbera heads. Blue rows show quantities derived from other parameters or emerging in the simulations.

References

D Anisimov, C Deng, and K Hormann. Subdividing barycentric coordinates. *Computer Aided Geometric Design*, 43:172–185, 2016.

E Bayer, RS Smith, T Mandel, N Nakayama, M Sauer, P Prusinkiewicz, and C Kuhlemeier. Integration of transport-based models for phyllotaxis and midvein formation. *Genes and Development*, 23:373–384, 2009.

M Cieslak, A Owens, and P Prusinkiewicz. Computational models of auxin-driven patterning in shoots. *Cold Spring Harbor Perspectives in Biology*, 14: a040097, 2022.

K Crane, F De Goes, M Desbrun, and P Schröder. Digital geometry processing with discrete exterior calculus. In *ACM SIGGRAPH 2013 Courses*, pages 1–126. 2013.

R Goldman. On the algebraic and geometric foundations of computer graphics. *ACM Transactions on Graphics*, 21:52–86, 2002.

G Guennebaud, B Jacob, et al. Eigen v3. http://eigen.tuxfamily.org, 2010.

A Jacobson. *Algorithms and interfaces for real-time deformation of 2D and 3D shapes*. PhD thesis, ETH Zurich, 2013.

A Jacobson, D Panozzo, et al. libigl: A simple C++ geometry processing library, 2018. https://libigl.github.io/.

H Jönsson, MG Heisler, BE Shapiro, EM Meyerowitz, and E Mjolsness. An auxin-driven polarized transport model for phyllotaxis. *Proceedings of the National Academy of Sciences, USA*, 103:1633–1638, 2006.

P Joshi, M Meyer, T DeRose, B Green, and T Sanocki. Harmonic coordinates for character articulation. *ACM Transactions on Graphics*, 26:71, pages 1–9, 2007.

N MacDonald. *Trees and Networks in Biological Models*. J. Wiley & Sons, Chichester, 1983.

GJ Mitchison. A model for vein formation in higher plants. *Proceedings of the Royal Society B*, 207:79–109, 1980.

CD Murray. A relationship between circumference and weight in trees and its bearing on branching angles. *The Journal of General Physiology*, 10:725–729, 1927.

DL O'Connor, A Runions, A Sluis, J Bragg, JP Vogel, P Prusinkiewicz, and S Hake. A division in pin-mediated auxin patterning during organ initiation in grasses. *PLoS Computational Biology*, 10:e1003447, 2014.

A Owens, M Cieslak, J Hart, R Classen-Bockhoff, and P Prusinkiewicz. Modeling dense inflorescences. *ACM Transactions on Graphics*, 35:136, pages 1–14, 2016.

D Reinhardt, ER Pesce, P Stieger, T Mandel, K Baltensperger, M Bennett, J Traas, J Friml, and C Kuhlemeier. Regulation of phyllotaxis by polar auxin transport. *Nature*, 426:255–260, 2003.

L Ringham, A Owens, M Cieslak, LD Harder, and P Prusinkiewicz. Modeling flower pigmentation patterns. *ACM Transactions on Graphics*, 40:233, pages 1–14, 2021.

Y Rodkaew, S Siripant, C Lursinsap, and P Chongstitvatana. An algorithm for generating vein images for realistic modeling of a leaf. In *Proceedings of the international conference on computational mathematics and modeling*, volume 9, pages 1–9, 2002.

Y Rodkaew, P Chongstitvatana, S Siripant, and C Lursinsap. Particle systems for plant modeling. In B-G Hu and M Jaeger, editors, *Plant growth modeling and applications. Proceedings of PMA03*, pages 210–217. Tsinghua University Press and Springer, Beijing, 2003.

A-G Rolland-Lagan and P Prusinkiewicz. Reviewing models of auxin canalization in the context of leaf vein pattern formation in Arabidopsis. *The Plant Journal*, 44:854–865, 2005.

A Runions, M Fuhrer, B Lane, P Federl, A-G Rolland-Lagan, and P Prusinkiewicz. Modeling and visualization of leaf venation patterns. *ACM Transactions on Graphics*, 24:702–711, 2005.

A Runions, B Lane, and P Prusinkiewicz. Modeling trees with a space colonization algorithm. In *Eurographics Workshop on Natural Phenomena 2007*, pages 63–70, 2007.

A Runions, M Tsiantis, and P Prusinkiewicz. A common developmental program can produce diverse leaf shapes. *New Phytologist*, 216:401–418, 2017.

T Sachs. Polarity and the induction of organized vascular tissues. *Annals of Botany*, 33:263–275, 1969.

T Sachs. *Pattern Formation in Plant Tissues*. Cambridge University Press, Cambridge, 1991.

JR Shewchuk. Triangle: Engineering a 2D Quality Mesh Generator and Delaunay Triangulator. In Ming C. Lin and Dinesh Manocha, editors, *Applied Computational Geometry: Towards Geometric Engineering*, volume 1148 of *Lecture Notes in Computer Science*, pages 203–222. Springer-Verlag, 1996.

RS Smith, S Guyomarc'h, T Mandel, D Reinhardt, C Kuhlemeier, and P Prusinkiewicz. A plausible model of phyllotaxis. *Proceedings of the National Academy of Sciences, USA*, 103:1301–1306, 2006.

D'Arcy Thompson. *On Growth and Form. Second Edition.* Cambridge University Press, Cambridge, 1942.

T Zhang, M Cieslak, A Owens, F Wang, SK Broholm, TH Teeri, P Elomaa, and P Prusinkiewicz. Phyllotactic patterning of gerbera flower heads. *Proceedings of the National Academy of Sciences, USA*, 118:e2016304118, 2021.